




## PAPER

[View Article Online](#)  
[View Journal](#) | [View Issue](#)Cite this: *Nanoscale Adv.*, 2022, 4, 3226Received 17th March 2022  
Accepted 22nd June 2022

DOI: 10.1039/d2na00166g

[rsc.li/nanoscale-advances](https://rsc.li/nanoscale-advances)Pressure-induced photoluminescence enhancement of CeF<sub>3</sub>:Tb<sup>3+</sup> nanoparticles†Tingting Zhao,<sup>a</sup> Xiaoling Jing,<sup>a</sup> Xueting Zhang,<sup>a</sup> Chenyi Li,<sup>a</sup> Ran Liu,<sup>a</sup> Bo Liu,<sup>a</sup> Chunxu Yang,<sup>a</sup> Longhai Shen,<sup>b</sup> <sup>\*b</sup> Qianjun Li <sup>\*a</sup> and Bingbing Liu <sup>a</sup>

Rare earth fluorides have been widely used in recent years in the field of solid-state lighting. However, the relationship between the structure and luminescence properties is still unclear. Herein, the photoluminescence and structural transition of CeF<sub>3</sub>:Tb<sup>3+</sup> nanoparticles under high pressure were investigated through *in situ* photoluminescence and X-ray diffraction measurements. Intriguingly, the photoluminescence of CeF<sub>3</sub>:Tb<sup>3+</sup> nanoparticles displays an enhancement from 18.3 to 33.4 GPa, accompanied by the phase transition from the starting hexagonal phase to the orthorhombic phase. It was found that the distance of luminescent centers increased sharply during the high-pressure phase transition, which weakened the quenching effect and improved transmission efficiency. Our work provides more insight into the optical characteristics and structures of rare earth trifluorides.

## Introduction

Rare earth (RE) trifluorides, as one of the famous families of functional materials, have attracted considerable attention because of their unique physical and chemical properties, such as low phonon energy, high resistivity, and high anionic conductivity.<sup>1,2</sup> These properties mentioned above are related to the luminescence of RE trifluorides. The light emission originates from the transitions between f-f or d-f electron states which depend on the local symmetry and structure of RE trifluorides.<sup>3,4</sup> Researchers had synthesized hexagonal GdF<sub>3</sub>:Eu<sup>3+</sup> nanocrystals that greatly enhanced Eu<sup>3+</sup> luminescence as compared to the orthorhombic ones.<sup>5</sup> However, it is still a great challenge to explore the influence of structures on the luminescence properties of rare earth fluorides with a large ionic radius (ranging from La to Nd) or small ionic radius (ranging from Tb to Lu, and Sm) due to the difficulty in synthesis of these materials with different crystal structures.<sup>6,7</sup>

It is well known that high pressure is an effective experimental means to change the local symmetry and structures. And many researchers had studied the luminescence properties of RE fluorides with different structures obtained by high pressure means. For example, Zou *et al.* discovered that the pressure-induced hexagonal phase of EuF<sub>3</sub> is beneficial to the enhancement of its photoluminescence (PL) intensity.<sup>8</sup> Li *et al.* observed the pressure enhanced PL intensity in ErF<sub>3</sub>, which is related to

its phase transition process from the orthorhombic structure to a hexagonal structure.<sup>9</sup> Gong *et al.* found that the Eu<sup>3+</sup> doped YF<sub>3</sub> nanocrystal PL also increased with the phase transition under pressure.<sup>10</sup> All the above indicate that high pressure is an effective method to regulate the structures and fluorescence properties of RE fluorides. However, there is no report on the relationship between the structure and luminescence properties of large radius RE fluorides.

As a main fluorescent material, compared with traditional oxide-based ones, the advantage of RE trifluorides lies in that their phonon vibration energy is fairly low, and RE ions as activators can be easily doped into the fluoride matrix.<sup>11</sup> Among various large radius rare-earth fluorides, the activator concentration of CeF<sub>3</sub> is 100%.<sup>12,13</sup> As we all know, CeF<sub>3</sub> experiences the phase transformation from the original hexagonal structure into an orthorhombic structure under high pressure.<sup>14,15</sup> This laid the foundation for us to further study the fluorescence characteristics of RE trifluorides under high pressure. Lanthanide(III)-doped nanocrystals have attracted great attention as a new kind of bioluminescent label.<sup>16</sup> Additionally, doped lanthanide ions can modify the optical properties, and thus different colored fluorescent labels can be generated by changing the dopants.<sup>17</sup> Doping Tb<sup>3+</sup> in CeF<sub>3</sub> brought out a strong green emission from Tb<sup>3+</sup> because of the efficient energy transfer from Ce<sup>3+</sup> to Tb<sup>3+</sup>.<sup>18–20</sup> As a potential scintillator and tunable laser material, CeF<sub>3</sub>:Tb<sup>3+</sup> nanoparticles also have the conjugate effect with biotin and avidin, which adds to the potential application with biomolecular fluorescent markers.<sup>12,13,21</sup> The investigation on the high-pressure behavior of CeF<sub>3</sub>:Tb<sup>3+</sup> nanocrystals would be pretty important for understanding the relationship between the structure and fluorescence characteristics of the REF<sub>3</sub> system.

<sup>a</sup>State Key Laboratory of Superhard Materials, Jilin University, Changchun 130012, P. R. China. E-mail: liquanjun@jlu.edu.cn

<sup>b</sup>School of Science, Shenyang Ligong University, Shenyang, 110159, China. E-mail: shenlonghai@163.com

† Electronic supplementary information (ESI) available. See <https://doi.org/10.1039/d2na00166g>

In this work, we explored the PL and the phase transitions of  $\text{CeF}_3\text{:Tb}^{3+}$  nanoparticles under high pressure using *in situ* PL and X-ray diffraction measurements. The hexagonal to orthorhombic phase transition and enhanced PL properties were discovered in  $\text{CeF}_3\text{:Tb}^{3+}$  nanoparticles under high pressure. These results provide new insight into the relationship between the structure and physical properties of RE trifluorides.

## Experimental

### Synthesis of $\text{CeF}_3\text{:Tb}^{3+}$ nanoparticles

The experimental method for the synthesis of  $\text{CeF}_3$  nanoplates is based on a previous report.<sup>20</sup>  $\text{CeF}_3\text{:Tb}^{3+}$  (1 mol%  $\text{Tb}^{3+}$ , 40 nm) nanoparticles were synthesized *via* a polyol process by employing diethylene glycol (DEG) as solvent. In brief, DEG containing  $\text{Tb}(\text{NO}_3)_3$  and  $\text{Ce}(\text{NO}_3)_3 \cdot 6\text{H}_2\text{O}$  was stirred and heated in a silicon oil bath in an argon atmosphere. At the same time,  $\text{NH}_4\text{F}$  was added to DEG in the oil bath. The obtained suspension was cooled to room temperature and diluted with 50 ml ethanol. The nanoparticles were obtained by centrifugation at a speed of 4500 rpm. Then they were redispersed in ethanol and centrifuged several times to remove the loosely adsorbed solvent molecules on their surfaces. Finally, the as-prepared samples were dried in air.

### High-pressure measurements

High-pressure experiments were performed by using a diamond anvil cell (DAC) with 400  $\mu\text{m}$  diameter culets. The samples and a ruby ball were loaded into a 120  $\mu\text{m}$  diameter hole drilled in

a steel gasket. The pressure was calibrated by the fluorescence emission of ruby.<sup>22</sup> Silicone oil was added into the hole as a pressure-transmitting medium. The high-pressure PL measurements were conducted using a home-built optical measurement system with a Horiba Jobin Yvon iHR320 spectrometer and a 360 nm light source. High-pressure X-ray diffraction experiments were performed by using a Rigaku Synergy Custom FR-X ( $\lambda = 0.7107 \text{ \AA}$ ). The XRD data were refined using the General Structure Analysis System (GSAS) program to obtain the lattice parameters.

## Results and discussion

### Characterization under ambient conditions

$\text{Tb}^{3+}$  doped hexagonal phase  $\text{CeF}_3$  with a doping concentration of 1% was synthesized *via* the polyol method.<sup>20</sup> From the low magnification TEM image (Fig. 1a), it can be seen that the  $\text{CeF}_3\text{:Tb}^{3+}$  sample is composed of nanoparticles. The average length of the particles is 40 nm. Fig. 1b clearly displays a well-resolved lattice fringe with a spacing of 0.16 nm, corresponding to the (114) plane of  $\text{CeF}_3$ , which indicates the high crystallinity of the sample. The energy dispersive X-ray analysis images (Fig. S1, ESI<sup>†</sup>) show that the  $\text{Tb}^{3+}$  ions are doped in  $\text{CeF}_3$ , and Fig. 1c (elemental mapping images) indicates that terbium and other elements are distributed uniformly in the  $\text{CeF}_3\text{:Tb}^{3+}$  nanoparticles. According to the previous literature, when  $\text{Tb}(\text{NO}_3)_3 \cdot 6\text{H}_2\text{O}$  was added as a raw material,  $\text{Tb}^{3+}$  is likely to substitute for  $\text{Ce}^{3+}$  in the  $\text{CeF}_3$  lattice.<sup>23</sup> It can be seen from Fig. 1d that  $\text{Tb}^{3+}$  ions occupied the  $\text{Ce}^{3+}$  sites in  $\text{CeF}_3\text{:Tb}^{3+}$  nanosized particles. The XRD

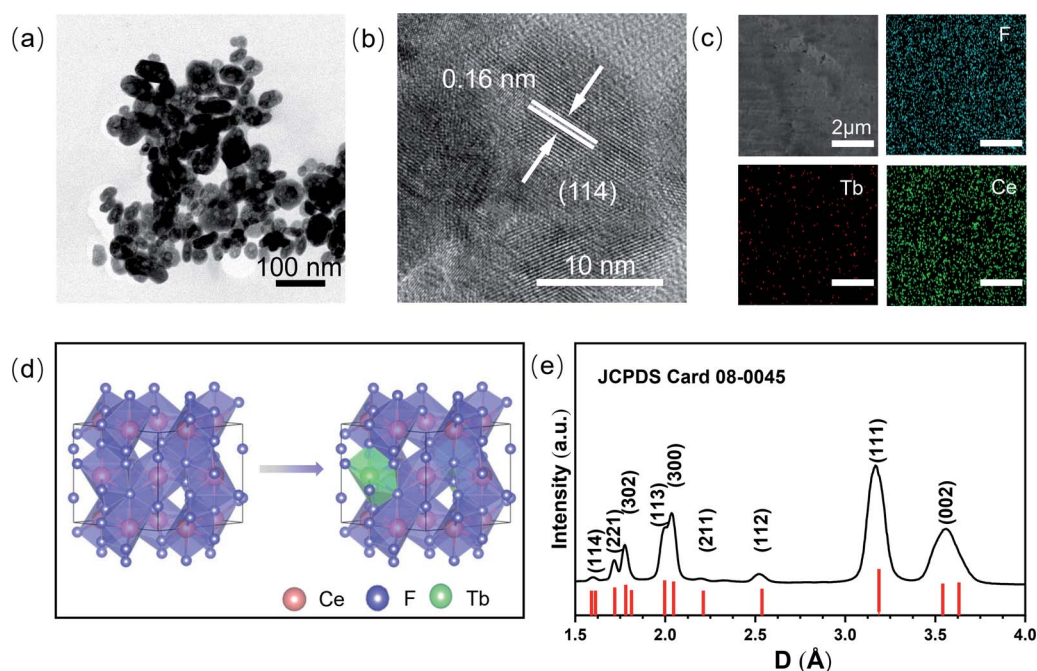
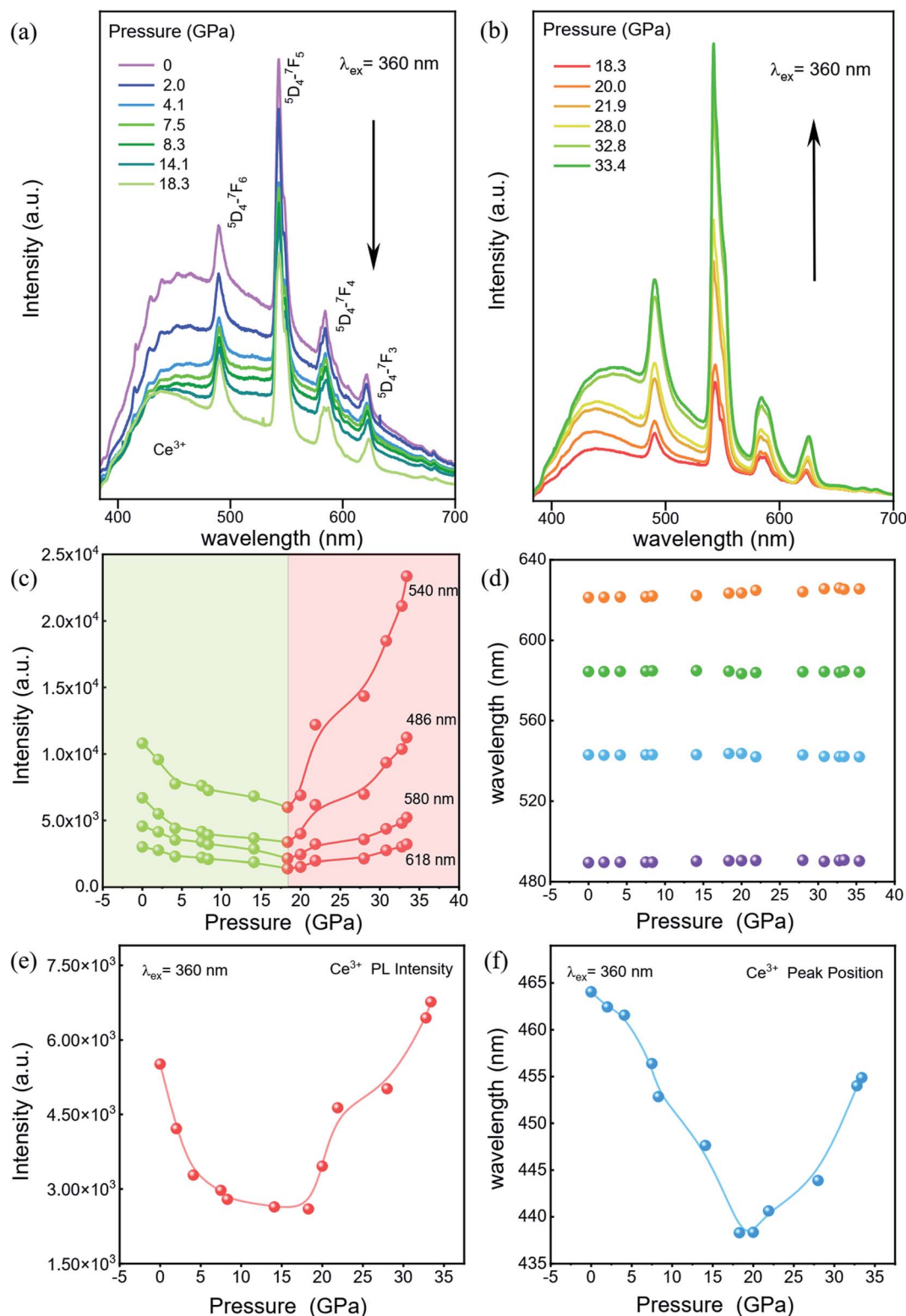


Fig. 1 Morphology characteristics of  $\text{CeF}_3$  nanoparticles doped with  $\text{Tb}^{3+}$  ions at ambient pressure. TEM micrographs at (a) low-resolution and (b) high-resolution. (c) Elemental mapping images of  $\text{Tb}^{3+}$  ion-doped  $\text{CeF}_3$  nanoparticles. (d) The polyhedral model before and after doping  $\text{Tb}^{3+}$  ions occupying the  $\text{Ce}^{3+}$  sites. (e) XRD patterns of the  $\text{CeF}_3\text{:Tb}^{3+}$  nanoparticles, and the standard data for bulk  $\text{CeF}_3$  (JCPDS Card No. 08-0045).



(Fig. 1e) results show that the sample is crystallized well, and all the peaks are consistent with the hexagonal structure of the bulk  $\text{CeF}_3$ .<sup>14</sup> The broadened XRD peaks of the  $\text{CeF}_3\text{:Tb}^{3+}$  sample are

due to the small size of the nanoparticles. The calculated lattice parameters of the  $\text{CeF}_3\text{:Tb}^{3+}$  nanoparticles ( $a = b = 0.710$  nm;  $c = 0.726$  nm) agree well with the reported values for  $\text{CeF}_3$  bulk.<sup>15</sup>



**Fig. 2** High-pressure PL properties of  $\text{CeF}_3\text{:Tb}^{3+}$ . (a) and (b) The PL spectrum changes of  $\text{CeF}_3\text{:Tb}^{3+}$  under pressure. Black arrows indicate the evolution of the PL spectra as a function of pressure. (c) Peak intensity, (d) Peak position evolution of  $\text{Tb}^{3+}$  ion-doped  $\text{CeF}_3$  nanoparticles at various pressures. (e) Peak intensity and (f) Peak position of  $\text{Ce}^{3+}$  at various pressures.



### In situ high-pressure optical and structural measurement

To explore the luminescent properties of  $\text{CeF}_3\text{:Tb}^{3+}$  nanoparticles, we carried out high-pressure PL experiments. As shown in Fig. 2a and b, five distinct peaks in the range of 380–700 nm are observed. The dominant sharp peaks ranging from 450–650 nm are assigned to the  $^5\text{D}_4 \rightarrow ^7\text{F}_j (j = 6-3)$  transition of  $\text{Tb}^{3+}$  ions; the band ranging from 384–680 nm is attributed to the 5d–4f transition of  $\text{Ce}^{3+}$ .<sup>20</sup> The  $\text{Ce}^{3+}$  PL intensities decrease monotonically with increasing the pressure up to 18.3 GPa (Fig. 2a). Upon further compression, the PL intensities of  $\text{Tb}^{3+}$  display an increasing trend up to 33.4 GPa (Fig. 2b), which enhanced by about twofold that of the starting pressure. At the same time, we can clearly see that the intensity of the 580 nm luminescence peak is enhanced more than that of the other luminescence peaks, which may be due to the more competitive transition of the  $^5\text{D}_4 \rightarrow ^7\text{F}_5$  energy level. It can be seen that no obvious shift occurred in the PL peak position (Fig. 2d). This is because the RE luminescence originates from the f–f electric dipole transitions of 4f electrons, which are shielded from environmental effects by the outer shell electrons. The pressure dependences of the  $\text{Ce}^{3+}$  PL position and intensity in our  $\text{CeF}_3\text{:Tb}^{3+}$  are shown in Fig. 2e and f. The PL of  $\text{Ce}^{3+}$  is attributed to the 5d–4f transition, which is not protected like the 4f shell anymore. So  $\text{Ce}^{3+}$  PL is vulnerable to external environmental impacts. We can see that the wavelength of  $\text{Ce}^{3+}$  shows

a blueshift upon increasing the pressure to 20 GPa and then displays a redshift upon increasing the pressure to 33.4 GPa. This intensity change of  $\text{Ce}^{3+}$  PL is roughly the same as that of  $\text{Tb}^{3+}$ , but the final increase is far less. This phenomenon may have originated from the energy transfer between  $\text{Ce}^{3+}$  and  $\text{Tb}^{3+}$ .<sup>20</sup>

We carried out high pressure XRD measurements to reveal the relationship of the structure–optical properties of the  $\text{CeF}_3\text{:Tb}^{3+}$  nanoparticles. The selected XRD patterns are shown in Fig. 3a. With increasing pressure, no apparent change is observed before 16.2 GPa, suggesting that the sample remained in the hexagonal phase. Upon further compression to 18.9 GPa, a new peak gradually appeared at around  $14^\circ$ , manifesting the beginning of a structural phase transition. We can clearly see the new diffraction peaks by peak fitting (Fig. 3b). And the structural phase transition process still progresses until 30.9 GPa. When released under ambient conditions, the structure of the sample returned to its initial phase. According to previous studies, we suggest that the new structural phase is the orthorhombic phase.<sup>23,24</sup> In the pressure range 18.9–30.9 GPa, the diffraction peaks of the hexagonal phase gradually weakened. And the intensities of the peaks belonging to the orthorhombic phase get stronger and stronger with increasing pressure, indicating the gradual transition from the hexagonal phase into the orthorhombic phase. Previous studies have shown that the particle size leads to a significant

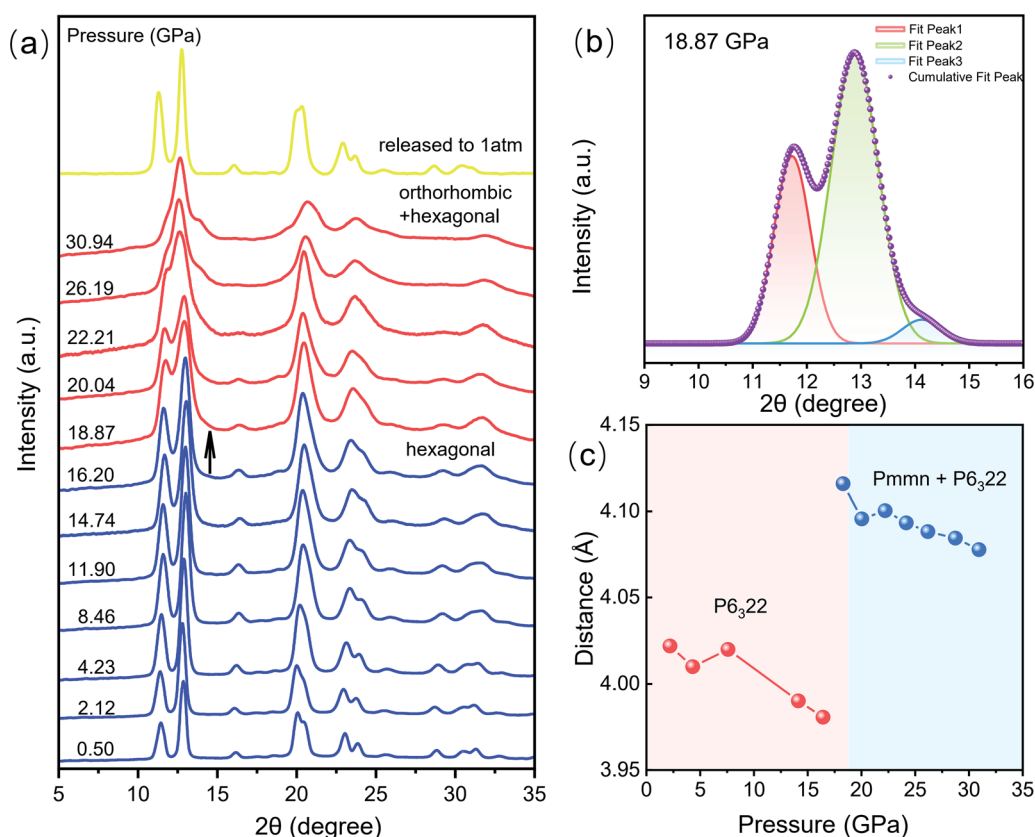
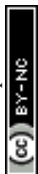


Fig. 3 Variation of structural information of  $\text{CeF}_3\text{:Tb}^{3+}$  nanoparticles at different pressures. (a) High-pressure XRD patterns of  $\text{CeF}_3\text{:Tb}^{3+}$  up to 30.9 GPa. (b) Origin peak fitting patterns of 18.9 GPa data. (c) Pressure dependences of the distance of Ce–Tb and Ce–Ce of  $\text{CeF}_3\text{:Tb}^{3+}$  nanoparticles.





decrease of the pressure in some nanomaterials because of the existence of the unstable cubic phase during the transition period from the hexagonal phase to the orthorhombic phase.<sup>15</sup> In addition, a small amount of  $\text{Tb}^{3+}$  dopant has a slight increase on the phase transition pressure although it does not affect the order of pressure-induced phase transition.<sup>25</sup> But on the whole, the phase transition pressure value of the materials is slightly lower than the bulk  $\text{CeF}_3$  phase transition value of 20.6 GPa.<sup>14</sup>

The length of Ce–Tb and Ce–Ce distance of  $\text{CeF}_3\text{:Tb}^{3+}$  nanoparticles were obtained by refining the diffraction patterns (Fig. 3c). Fig. S2† shows Rietveld refinement of the diffraction pattern of  $\text{CeF}_3\text{:Tb}^{3+}$  at 18.9 GPa. In the pressure range 2.1–16.2 GPa, the distances between Ce–Tb and Ce–Ce decrease gradually with increasing pressure. But the distances increase significantly above 16.2 GPa accompanied by the structural phase transition. Upon further compression, the Ce–Tb and Ce–Ce distances are reduced steadily up to the highest

experimental pressure of 30.9 GPa, but they are still much larger than those of the starting phase in the low-pressure range.

## Discussion

Under 360 nm UV light irradiation,  $\text{CeF}_3\text{:Tb}^{3+}$  nanoparticles exhibit bright green emission at atmospheric pressure. Fig. 4a and b show the energy transfer process and the emission spectra of the sample, respectively.<sup>20,26,27</sup> The emission spectra consist of a broad band and several peaks. The band located in the range 384–680 nm is ascribed to the 5d–4f transition of  $\text{Ce}^{3+}$ . The strong sharp peaks between 450 and 650 nm (peaking at 489, 543, 584 and 618 nm), emission of  $\text{Tb}^{3+}$ , derive from transitions between the excited  $^5\text{D}_4$  state and the  $^7\text{F}_j$  ( $j = 6-3$ ) ground states of  $\text{Tb}^{3+}$  ions.<sup>26</sup> Energy transfer takes a critical part in improving the emission efficiency of RE materials. The energy transfer process from  $\text{Ce}^{3+}$  to  $\text{Tb}^{3+}$  takes place by

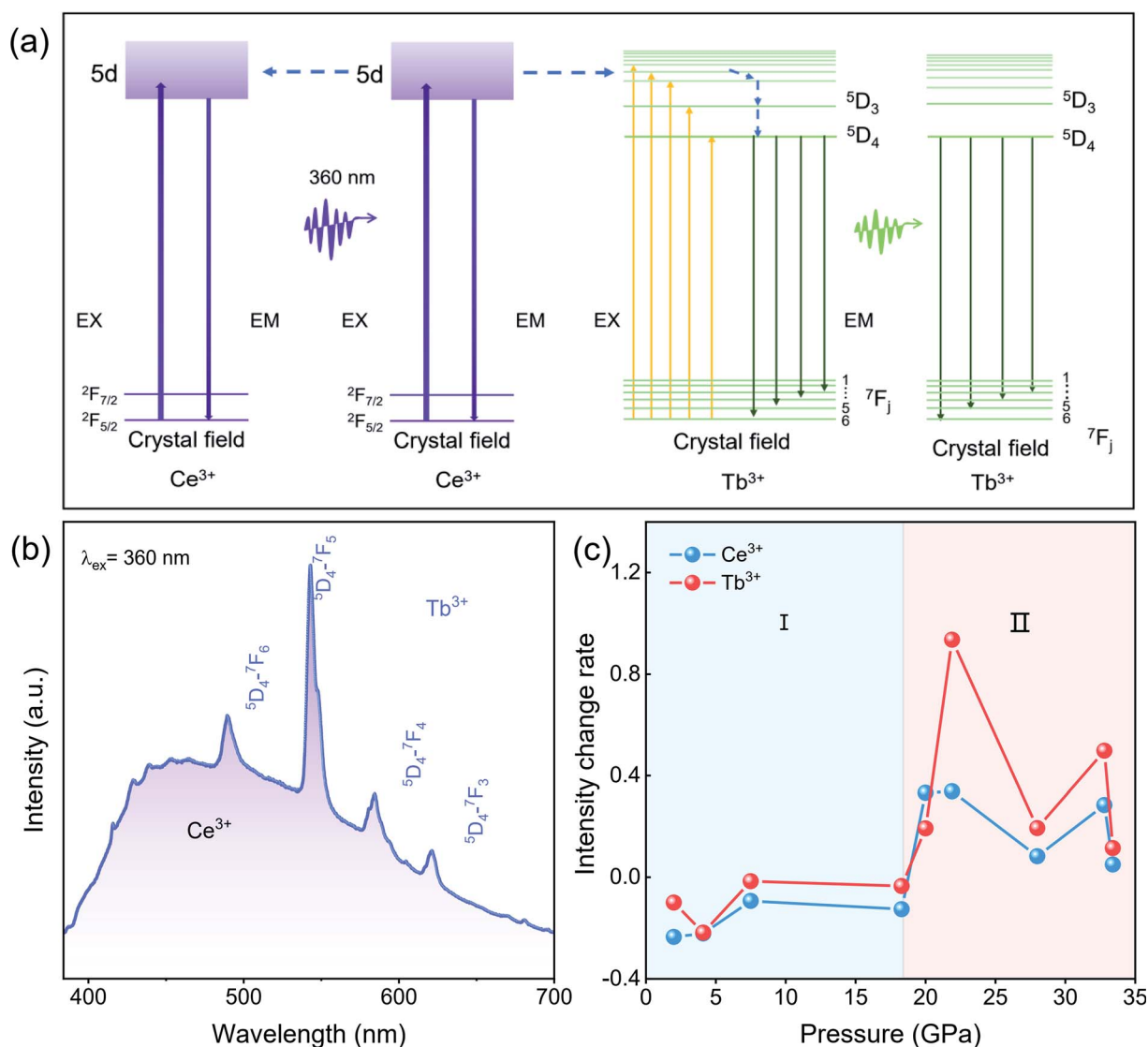


Fig. 4 Luminescent properties of  $\text{CeF}_3\text{:Tb}^{3+}$ . (a) Energy level scheme of  $\text{CeF}_3\text{:Tb}^{3+}$  with electronic transitions and energy transfer processes. (b) The PL spectra of  $\text{CeF}_3\text{:Tb}^{3+}$  at ambient pressure. (c) The rate of intensity changes for  $\text{Ce}^{3+}$  and  $\text{Tb}^{3+}$  with pressure.



resonance transfer (electric dipole-electric quadrupole interaction) upon excitation with UV light. For the  $\text{CeF}_3$  system, first,  $\text{Ce}^{3+}$  ions are excited by UV light excitation; subsequently, energy transfer occurs from  $\text{Ce}^{3+}$  to  $\text{Tb}^{3+}$  ions.<sup>28–30</sup>

According to the energy transfer process between  $\text{Ce}^{3+}$  and  $\text{Tb}^{3+}$  at atmospheric pressure (Fig. 4b), we know that the distance between luminescent centers is crucial to the luminescence of RE fluorides, such as concentration quenching phenomena.<sup>31,32</sup> In energy transfer processes of  $\text{CeF}_3:\text{Tb}^{3+}$  under ambient pressure, there is a cascade transfer process between  $\text{Ce}^{3+}$  and  $\text{Ce}^{3+}$ , that is, energy can be transferred from  $\text{Ce}^{3+}$  to another  $\text{Ce}^{3+}$  or a quenching center except for energy transfer between  $\text{Ce}^{3+}$  and  $\text{Tb}^{3+}$ .<sup>32</sup> When the distance between  $\text{Ce}^{3+}$  and  $\text{Ce}^{3+}$  is close to a certain extent, a cascade transfer process occurs between  $\text{Ce}^{3+}$  and  $\text{Ce}^{3+}$ . And the excitation energy is likely to be transferred to the quenching centers, resulting in energy loss. Considering the decrease of the distance between the luminescence centers from the XRD refinement result (Fig. 3c), it is reasonable to assume that the distance between the luminous centers in the starting hexagonal phase  $\text{CeF}_3:\text{Tb}^{3+}$  is less than the critical value where PL quenching begins. Therefore, the decreased PL intensity in the range of 0–18.3 GPa can be attributed to the decrease in the distance between the luminescence centers, which results in the loss of partially excited light. Similarly,  $\text{Tb}^{3+}$  ions gradually approach each other with increasing pressure, and energy migration also takes place between these ions like  $\text{Ce}^{3+}$ , which adds to the energy loss through easier access to quenching centers.<sup>25</sup>

Above 18.3 GPa, the PL intensity of the  $\text{CeF}_3:\text{Tb}^{3+}$  nanoparticles display a clear increase with increasing pressure, which is also related to the distance between the luminescence centers. The distance between luminescence centers in the high-pressure orthorhombic phase decreases slowly, but it is larger than that of the starting phase, resulting in the suppression of the quenching phenomenon between the luminescent centers. According to the intensity change rate diagram (Fig. 4c), we can see that the relative intensity changes of  $\text{Tb}^{3+}$  are much larger than those of  $\text{Ce}^{3+}$  after 20.0 GPa, which means that apart from the fact that partial excited  $\text{Ce}^{3+}$  passes energy to  $\text{Tb}^{3+}$  instead of conducting the emission process, the nonradiative-relaxation processes down towards the  $^5\text{D}_4$  state of  $\text{Tb}^{3+}$  might probably be simplified as well due to the red shift of  $\text{Ce}^{3+}$  (Fig. 2f). From another angle, the thus benefited  $^5\text{D}_4 \rightarrow ^7\text{F}_j$  ( $j = 6-3$ ) transition can better compete with other unwanted energy pathways like those from excited  $\text{Ce}^{3+}$  or  $\text{Tb}^{3+}$  to quenching centers, further promoting the PL. Therefore, the enhanced luminescence intensity in the high-pressure phase is due to the weakened quenching effect and improved transmission efficiency. From the above analysis, we suggest that an ideal distance between RE ions in materials is significantly important for high-quality PL, and high pressure is undoubtedly an effective method to modulate the PL properties through phase engineering.

## Conclusions

In summary, we investigated the photoluminescence properties and structural transition of  $\text{CeF}_3:\text{Tb}^{3+}$  nanoparticles by *in situ*

PL and XRD measurements under high pressure. The  $\text{CeF}_3:\text{Tb}^{3+}$  nanoparticles undergo the structural phase transition from the starting hexagonal phase to an orthorhombic phase at 18.9 GPa with the distance between the luminescence centers increasing sharply and then slowly decreasing. The PL intensity of the  $\text{CeF}_3:\text{Tb}^{3+}$  nanoparticles decreases between 0–18.3 GPa, which is due to the fact that the decrease in the distance between the luminescence centers results in the loss of partially excited light. With increasing pressure, the fluorescence intensity increases until 33.4 GPa, which is related to the change of the distance between the luminescence centers, which diminishes the negative quenching effect and improves transmission efficiency. The results provide a deep understanding of the relationship between the structure and fluorescence characteristics of RE fluorides.

## Conflicts of interest

There are no conflicts to declare.

## Acknowledgements

This work was financially supported by the National Key Research and Development Program of China (No. 2018YFA0305900), National Natural Science Foundation of China (11874172, U2032215 and 11634004), and JLU Science and Technology Innovative Research Team (2017TD-01).

## Notes and references

- 1 L. Wang, P. Li and Y. Li, *Adv. Mater.*, 2007, **19**, 3304–3307.
- 2 C. G. Olson, M. Piacentini and D. W. Lynch, *Phys. Rev. B*, 1978, **18**, 5740–5749.
- 3 F. Meiser, C. Cortez and F. Caruso, *Angew. Chem., Int. Ed. Engl.*, 2004, **43**, 5954–5957.
- 4 F. Wang, W. B. Tan, Y. Zhang, X. Fan and M. Wang, *Nanotechnology*, 2006, **17**, R1–R13.
- 5 X. Zhang, T. Hayakawa, M. Nogami and Y. Ishikawa, *J. Alloys Compd.*, 2011, **509**, 2076–2080.
- 6 Z. Allan, T. H. David and H. E. Ted, *Inorg. Chem.*, 1966, **5**(8), 1466–1468.
- 7 V. M. Mansnmann, *Z. Anorg. Allg. Chem.*, 1964, **331**, 98–101.
- 8 Q. Li, S. Li, K. Wang, J. Liu, B. Liu, K. Yang and B. Zou, *J. Phys. Chem. C*, 2014, **118**, 7562–7568.
- 9 W. Li, X. Ren, Y. Huang, Z. Yu, Z. Mi, N. Tamura, X. Li, F. Peng and L. Wang, *Solid State Commun.*, 2016, **242**, 30–35.
- 10 C. Gong, Q. Li, R. Liu, Y. Hou, J. Wang, X. Dong, B. Liu, X. Tan, J. Liu, K. Yang, B. Zou, T. Cui and B. Liu, *J. Phys. Chem. C*, 2014, **118**, 22739–22745.
- 11 C. M. B. Bender and J. M., *Chem. Mater.*, 2000, **12**, 1969–1976.
- 12 A. J. Wojtowicz, M. Balcerzyk, E. Berman and A. Lempicki, *Phys. Rev. B*, 1994, **49**, 14880–14895.
- 13 G. G. Blasse and B. C., *Springer:Berlin*, 1994, 1–232.
- 14 T. I. Dyuzheva, L. M. L., G. B. Demishev and N. A. Bendeliani, *Inorg. Mater.*, 2003, **39**, 1198–1202.
- 15 P. Wang, Q. J. Li, R. Liu, M. G. Yao, D. M. Li, B. Zou, T. Cui, J. Liu, Z. Q. Chen and B. B. Liu, *J. Appl. Phys.*, 2012, **111**, 1–4.



- 16 F. Wang, Y. Zhang, X. Fan and M. Wang, *Nanotechnology*, 2006, **17**, 1527–1532.
- 17 R. B. Cédric Louis, C. A. Marquette, J.-L. Bridot, S. Roux, G. Ledoux, B. Mercier, L. Blum, P. Pascal and O. Tillement, *Chem. Mater.*, 2005, **17**, 1673–1682.
- 18 J. W. Stouwdam and F. van Veggel, *Langmuir*, 2004, **20**, 11763–11771.
- 19 M. H. Riwozki K, A. Kornowski and M. Haase, *J. Phys. Chem. B*, 2000, **104**, 2824.
- 20 Z. W. Q. Z. L. Wang and P. Y. Jia, *Chem. Mater.*, 2006, **18**, 2030–2037.
- 21 D. Y. Kong, Z. L. Wang, C. K. Lin, Z. W. Quan, Y. Y. Li, C. X. Li and J. Lin, *Nanotechnology*, 2007, **18**, 075601.
- 22 H. K. Mao, J. Xu and P. M. Bell, *J. Geophys. Res.: Atmos.*, 1986, **91**, 4673–4676.
- 23 X. Li, W. Zhang, L. Dong, D. Liu and Z. Qi, *J. Lumin.*, 2019, **205**, 122–128.
- 24 W. A. Crichton, P. Bouvier, B. Winkler and A. Grzechnik, *Dalton Trans.*, 2010, **39**, 4302–4311.
- 25 C. Gong, Q. Li, R. Liu, Y. Hou, J. Wang, X. Dong, B. Liu, X. Yang, Z. Yao, X. Tan, D. Li, J. Liu, Z. Chen, B. Zou, T. Cui and B. Liu, *Phys. Chem. Chem. Phys.*, 2013, **15**, 19925–19931.
- 26 D. Wang and N. Kodama, *J. Solid State Chem.*, 2009, **182**, 2219–2224.
- 27 H. Guo, *Appl. Phys. B*, 2006, **84**, 365–369.
- 28 G. Blasse and A. Bril, *J. Chem. Phys.*, 1969, **51**, 3252–3254.
- 29 J. C. Bourcet and F. K. Fong, *J. Chem. Phys.*, 1974, **60**, 34–39.
- 30 Z. Wang, Z. Quan, J. Lin and J. Fang, *J. Nanosci. Nanotechnol.*, 2005, **5**, 1532–1536.
- 31 D. L. Dexter and J. H. Schulman, *J. Chem. Phys.*, 1954, **22**, 1063–1070.
- 32 D. J. Shi Chaoshu, W. Yaguang, *et al.*, *Chin. Phys. Lett.*, 2000, **17**(7), 532–533.

